

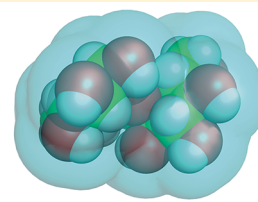
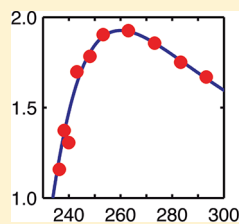
# Hydration and Mobility of Trehalose in Aqueous Solution

Louise Revsbech Winther, Johan Qvist, and Bertil Halle\*

Department of Biophysical Chemistry, Center for Molecular Protein Science, Lund University, SE-22100 Lund, Sweden

## S Supporting Information

**ABSTRACT:** The disaccharide trehalose stabilizes proteins against unfolding, but the underlying mechanism is not well understood. Because trehalose is preferentially excluded from the protein surface, it is of interest to examine how trehalose modifies the structure and dynamics of the solvent. From the spin relaxation rates of deuterated trehalose and  $^{17}\text{O}$ -enriched water, we obtain the rotational dynamics of trehalose and water in solutions over wide ranges of concentration (0.025–1.5 M) and temperature (236–293 K). The results reveal direct solute–solute interactions at all concentrations, consistent with transient trehalose clusters. Similar to other organic solutes, the trehalose perturbation of water rotation (and hydrogen-bond exchange) is modest: a factor 1.6 (at 298 K) on average for the 47 water molecules in the first hydration layer. The deviation of the solute tumbling time from the Stokes–Einstein–Debye relation is partly caused by a dynamic solvent effect that is often modeled by incorporating “bound water” in the hydrodynamic volume. By comparing the measured temperature dependences of trehalose and water dynamics, we demonstrate that a more realistic local viscosity model accounts for this second-order dynamic coupling.



## INTRODUCTION

Trehalose, a disaccharide composed of two  $\alpha$ -(1 $\leftrightarrow$ 1)- $\alpha$  linked D-glucose units, protects a variety of organisms against environmental stress.<sup>1–3</sup> For example, it is the principal endogenous osmolyte produced by *E. coli* to maintain turgor pressure in hyperosmotic environments.<sup>4</sup> Trehalose can accumulate to high levels without interfering with cell function because it does not interact directly with vital cell components. In fact, the preferential exclusion of trehalose from biological interfaces (at ambient temperature) has the effect of stabilizing proteins against unfolding<sup>5,6</sup> by a mechanism that is not fully understood.<sup>7,8</sup> Trehalose accumulation to even higher levels, up to 20% of the organism's dry mass, allows certain microbes, invertebrates, and lower plants to survive almost complete dehydration in a metabolically dormant state.<sup>9</sup> The mechanisms whereby trehalose preserves the viability of highly desiccated cells must be entirely different from its osmoprotectant mechanism. Rather than being excluded from protein surfaces, trehalose replaces water as a H-bond partner<sup>9</sup> and, in some cases, it induces a glass transition in the cytoplasm.<sup>10–12</sup> Trehalose is also widely used to stabilize protein drugs, vaccines and bacteria during freeze-drying and storage.<sup>13,14</sup>

Trehalose is not unique in accomplishing these feats; bacteria employ a diverse range of osmoprotectants<sup>15,16</sup> and higher plants accumulate sucrose during anhydrobiosis.<sup>17</sup> Nevertheless, the widespread occurrence in nature of trehalose as a stabilizer of biological structures has fuelled a long-standing search for physicochemical properties of trehalose that might provide clues to the mechanisms involved. Both trehalose and sucrose are chemically inert (nonreducing) sugars. Trehalose has an exceptionally high glass transition temperature of 115 °C (in the absence of water),<sup>18</sup> and the  $\alpha$ -(1 $\leftrightarrow$ 1)- $\alpha$  glycosidic linkage confers a high degree of rigidity to the molecule despite

the lack of intramolecular H-bonds.<sup>19</sup> But the property most often implicated in the protein-stabilizing effect of trehalose is its interaction with water. If trehalose is preferentially excluded from the protein surface, the mechanism must be indirect<sup>20–22</sup> and it is thus imperative to examine how trehalose perturbs the H-bond network of the surrounding solvent.

For these reasons, the physical properties of aqueous trehalose solutions have been investigated by numerous techniques, including nuclear spin relaxation of water<sup>23,24</sup> and trehalose,<sup>24,25</sup> dielectric spectroscopy,<sup>26,27</sup> depolarized light scattering,<sup>28,29</sup> vibrational spectroscopy,<sup>30,31</sup> quasielastic neutron scattering,<sup>32–34</sup> neutron diffraction<sup>35</sup> and molecular dynamics simulations.<sup>19,36–43</sup> These studies have yielded many important insights, but the emerging picture is not clear-cut. In particular, there is still disagreement about the range and extent of solvent perturbation by trehalose.

Trehalose interacts with the surrounding water primarily via its 8 hydroxyl groups,<sup>36–39,41,43</sup> which also may mediate direct trehalose–trehalose contacts.<sup>40,42</sup> To elucidate the dynamics of trehalose solutions, it is therefore desirable to monitor trehalose and water simultaneously. In the present work, this was accomplished by nuclear spin relaxation measurements on deuterated trehalose in  $^{17}\text{O}$ -enriched water. We thus report trehalose  $^2\text{H}$  and water  $^{17}\text{O}$  spin relaxation data over wide ranges of concentration (0.025–1.47 M) and temperature (236–293 K). Oxygen-17 is the NMR nuclide of choice for selectively probing water in solutions where the solute contains labile hydrogens that would contribute to the  $^2\text{H}$  signal in a  $\text{D}_2\text{O}$  solution.<sup>24</sup> Compared to existing water  $^{17}\text{O}$  data from

Received: May 22, 2012

Revised: June 28, 2012

trehalose solutions,<sup>23</sup> the present data represent a substantial improvement in accuracy and in the range of investigated solution conditions. Freezing of the solvent in the supercooled regime was prevented by dispersing the solution in  $\mu\text{m}$ -sized emulsion droplets that are large enough that the oil–water interface has negligible effect but small enough to allow supercooling to near the homogeneous nucleation temperature.<sup>44,45</sup> Trehalose dynamics was monitored via  $^2\text{H}$  relaxation, which is preferable to  $^{13}\text{C}$  relaxation<sup>24,25</sup> because of the faster relaxation (permitting accurate measurements also on dilute solutions) and because the hydrocarbon phase in emulsion samples does not contribute to the  $^2\text{H}$  signal.

The data presented here accurately characterize the rotational dynamics of trehalose and of the water molecules in its hydration layer over wide ranges of concentration and temperature. In addition, they demonstrate a second-order dynamic coupling where the tumbling of the solute is slowed down because it creates a more viscous solvent around itself. We argue that our dynamic description of this correction to the standard hydrodynamic picture (based on the Stokes–Einstein–Debye relation) is more appropriate than the common “iceberg” picture, where a certain number of “immobilized” solvent molecules are incorporated in the hydrodynamic volume of the solute.

According to our results, the hydration of trehalose is unremarkable and fully in line with that of other small organic solutes when hydration layers (or hydration numbers) are defined in a consistent way.<sup>45</sup> We argue that our results, as well as results obtained by others and interpreted otherwise, are consistent with a short-ranged hydration effect, where the dynamic perturbation is essentially confined to the water molecules interacting directly with the solute. Trehalose self-association, studied previously primarily by MD simulations (which may be biased by force-field imperfections), are unambiguously demonstrated here at all examined concentrations.

## MATERIALS AND METHODS

**Sample Preparation.**  $\alpha,\alpha$ -Trehalose dihydrate ( $\geq 99.0\%$  purity, Fluka) was partially deuterated in carbon positions 2, 3, 4, and 6 using Raney nickel as catalyst (Raney 4200 slurry, Aldrich) in  $\text{D}_2\text{O}$  (99.8 atom %, Cortecnet).<sup>46</sup> The purity of the reaction product was checked by anion exchange chromatography and the degree of deuteration was determined by  $^1\text{H}$  NMR spectroscopy (Supporting Information S1). The residual (after Chelex treatment) Ni(II) concentration in the trehalose solutions, determined by mass spectrometry, was sufficiently low to have a negligible (paramagnetic) effect on the water  $^{17}\text{O}$  relaxation (Supporting Information S2).

Partially deuterated trehalose was dissolved in a water mixture made from Ultra pure  $\text{H}_2\text{O}$  (Fluka) and  $^{17}\text{O}$ -enriched  $\text{H}_2\text{O}$  (21 atom %  $^{17}\text{O}$ , Icon) to a final  $^{17}\text{O}$  level of 0.5 atom %. All samples were centrifuged at 13 000 rpm for 10 min, retaining the supernatant. The trehalose concentration was determined by  $^{13}\text{C}$  NMR spectroscopy with isobutanol as internal standard (Supporting Information S3). The water/trehalose mole ratio  $N_{\text{W}}$  was obtained from the molar concentration and apparent partial molar volume of trehalose (Supporting Information S3).

Relaxation measurements at temperatures below the equilibrium freezing point of  $\text{H}_2\text{O}$  were performed on emulsion samples,<sup>44</sup> prepared by mixing  $\sim 1$  mL trehalose solution with an equal volume of *n*-heptane ( $>99\%$ , HPLC grade, Sigma)

containing 3% (w/w) of the nonionic emulsifier sorbitan tristearate (Sigma). A water-in-oil emulsion with aqueous droplet diameter in the range 1–15  $\mu\text{m}$  was obtained by mixing the two solutions, heated to  $\sim 50^\circ\text{C}$ , with the aid of two 5 mL syringes connected via a 0.56 mm i.d. nozzle (Hamilton) and pressing the mixture through the nozzle  $\sim 70$  times. All emulsion samples were stored at  $5^\circ\text{C}$  until used. Within experimental accuracy, the  $^2\text{H}$  and  $^{17}\text{O}$   $R_1$  values measured on emulsion samples were identical to the  $R_1$  values measured on conventional (nonemulsified) samples at the same temperature and concentration (Supporting Information S4). The ice signal from the small fraction of water droplets that freeze by heterogeneous nucleation at temperatures below  $0^\circ\text{C}$  is broadened beyond detection and does not affect the  $R_1$  measurement.

**Magnetic Relaxation Measurements.** The  $^2\text{H}$  (trehalose) and  $^{17}\text{O}$  (water) longitudinal relaxation rate  $R_1$  was measured with a Varian VnmrS Direct-Drive spectrometer operating at 92.1 or 81.3 MHz, respectively.  $R_1$  was determined from 3-parameter fits to single-exponential inversion–recovery curves with 30–40 delay times and a sufficient number of transients to obtain a signal-to-noise ratio larger than 100. For  $^2\text{H}$ , a small peak due to residual water deuterons was computationally removed before integrating the main trehalose  $^2\text{H}$  peak. (At the highest trehalose concentration, the water  $^2\text{H}$  peak corresponds to a concentration of about twice the natural abundance.) For  $^{17}\text{O}$ , a pure water reference sample was also measured after each sample. The sample temperature was controlled with a regulated flow of dry air and was measured before and after each series of relaxation measurements at a given temperature with a copper–constantan thermocouple (in an NMR tube containing a water–ethanol mixture) referenced to an ice–water bath. The standard deviation in the temperature was  $<0.1$  K above 273 K, 0.1–0.2 K down to 238 and 0.3 K at the lowest temperature 236 K). On the basis of repeated measurements, the accuracy in  $^2\text{H}$  and  $^{17}\text{O}$   $R_1$  values was estimated to 2% at the two lowest temperatures (236 and 238 K) and to 1% at all other temperatures. However, for the most dilute (50 mM) sample, the accuracy in  $^2\text{H}$   $R_1$  was estimated to 3% at all examined temperatures.

## RESULTS AND DISCUSSION

**Trehalose Tumbling.** To monitor solute and solvent dynamics in the same sample, trehalose was (partially) deuterated in five nonlabile positions (Figure 1). On average, each trehalose molecule carries 3.5 deuterons, 75% of which are attached to ring carbons whereas 25% belong to the exocyclic methylene group (Supporting Information S1). The longitudinal relaxation rate  $R_1$  of the trehalose  $^2\text{H}$  magnetization was measured as a function of trehalose concentration (0.025–1.47 M) at 293 K (Figure 2) and as a function of temperature (236–293 K) at four concentrations in the range 50–249 mM (Figure 3). To avoid freezing at subzero temperatures, the temperature dependence was measured on emulsified samples (see Materials and Methods).

$^2\text{H}$  relaxation is induced by reorientational motions that modulate the  $^2\text{H}$  nuclear electric quadrupole coupling.<sup>47</sup> To a good approximation, the  $^2\text{H}$  electric field gradient tensor is axially symmetric with the largest principal component along the C–D bond.<sup>48</sup> The trehalose molecule adopts a single preferred conformation in solution,<sup>19,25,49</sup> virtually identical to the crystal structure of the dihydrate<sup>50</sup> (Figure 1). Comparing

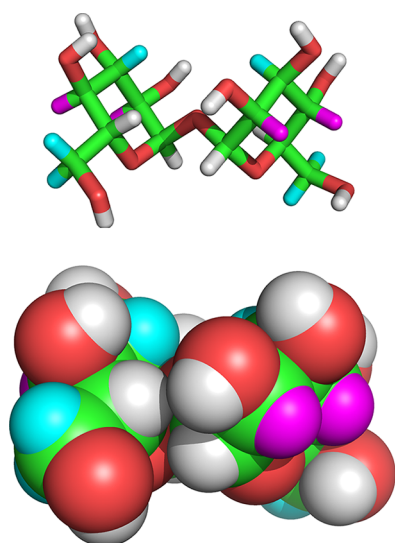


**Figure 1.** Trehalose in stick and van der Waals representation with the partially deuterated hydrogen positions indicated: HC2 and HC4 (magenta, 51–56% deuteration), and HC3 and H<sub>2</sub>C6 (cyan, 22–24% deuteration). The trehalose dihydrate crystal structure<sup>50</sup> shown here is closely similar to the dominant solution structure.<sup>19,25,49</sup>

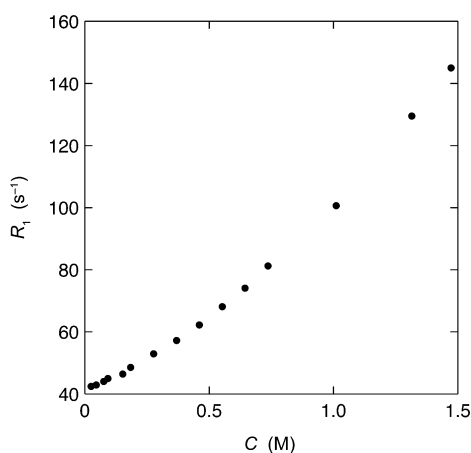


**Figure 2.** Trehalose <sup>2</sup>H longitudinal relaxation rate  $R_1$  at 92.1 MHz versus trehalose concentration in aqueous solution at 293.2 K. Error bars are smaller than or comparable to the symbol size.

the crystal structure of trehalose dihydrate<sup>50</sup> with the crystal structure of trehalose loosely associated with the protein ricin (PDB ID 1j1m), we find a root-mean-square deviation of 0.23 Å for the 12 ring atoms plus the glycosidic oxygen and 0.32 Å for all 22 non-H atoms except one of the exocyclic O6 atoms, which occupies different torsional minima in the two structures.

The modulation of the quadrupole coupling is mainly due to molecular tumbling, but internal motions (C–D bond librations and torsional vibrations of the hydroxymethyl group) may also contribute. Previous <sup>13</sup>C relaxation studies of trehalose<sup>25</sup> and sucrose<sup>51–54</sup> solutions have shown that the internal motions are sufficiently fast that their direct contribution to  $R_1$  is negligible. (Because the internal motions have a weaker temperature dependence than the overall tumbling, this approximation is even more justified in the supercooled regime.) Nevertheless,  $R_1$  is affected by the amplitude of the internal motions via the orientational order parameter  $S^2$  of the C–D bond. This parameter specifies the fraction of the time correlation function that decays by

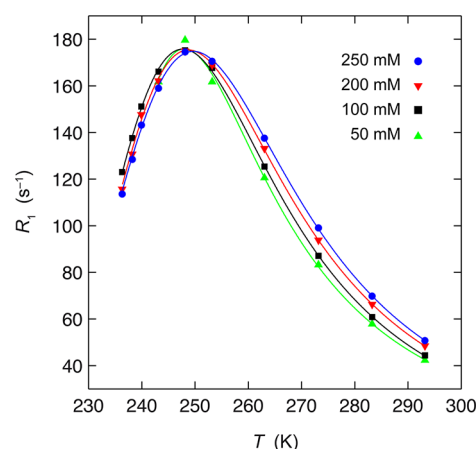


**Figure 3.** Trehalose <sup>2</sup>H longitudinal relaxation rate  $R_1$  at 92.1 MHz versus temperature in aqueous solutions at four trehalose concentrations. Error bars are smaller than the symbol size, except at 50 mM. Each curve resulted from a 4-parameter fit as described in the text.

molecular tumbling and  $1 - S^2$  may be regarded as a measure of the internal-motion amplitude. Previous <sup>13</sup>C studies<sup>25,51–54</sup> indicate that the disaccharide tumbles as a spherical top, at least at the low concentrations examined in Figure 3. Consistent with this result, atomic-level hydrodynamic calculations<sup>55</sup> based on a crystal structure of trehalose (PDB ID 1j1m) show that the span of the 5 asymmetric-top rotational correlation times is merely 20%, too small to be experimentally resolved.

Under these conditions, the <sup>2</sup>H relaxation rate can be expressed as<sup>47,56</sup>

$$R_1 = (\omega_Q S)^2 \frac{1}{5} \left[ \frac{\tau_R}{1 + (\omega_0 \tau_R)^2} + \frac{4\tau_R}{1 + (2\omega_0 \tau_R)^2} \right] \quad (1)$$

where  $\omega_Q$  is the <sup>2</sup>H quadrupole frequency and  $\omega_0 = 2\pi\nu_0 = 5.787 \times 10^8 \text{ rad s}^{-1}$  is the <sup>2</sup>H Larmor (angular) frequency in a magnetic field of 14.1 T. The quadrupole frequency  $\omega_Q$  and the order parameter  $S^2$  may vary among the five deuterated positions, but any such variation must be small because we could not detect any deviation from exponential inversion recovery of the total observed <sup>2</sup>H magnetization. Henceforth, we shall therefore regard  $\omega_Q$  and  $S^2$  as effective averages over the labeled sites.

The quadrupole frequency is largely governed by the C–D bond length so  $\omega_Q$  should not vary with temperature. Furthermore, at least in the temperature range examined here, the order parameter  $S^2$  should only depend weakly on temperature, as found for the closely related <sup>13</sup>C order parameter.<sup>25,51–54</sup> In this approximation, the observed temperature dependence in  $R_1$  can be attributed solely to the tumbling time  $\tau_R$ . To analyze the data in Figure 3, the function  $\tau_R(T)$  must be specified. At the low concentrations in Figure 3,  $\tau_R$  is expected (see below) to scale approximately as  $\eta_0/T$ , where  $\eta_0$  is the viscosity of the H<sub>2</sub>O solvent. At low temperatures,  $\eta_0(T)$  deviates strongly from the Arrhenius law,<sup>57,58</sup> but it can be accurately represented by a fractional power law.<sup>59</sup> We thus write  $\tau_R(T) = \tau_R^0(T/T_0 - 1)^{-\gamma}$ . Inserting this form into eq 1, we obtain an expression for  $R_1(T)$  with four parameters:  $(\omega_Q S)^2$ ,  $\tau_R^0$ ,  $T_0$ , and  $\gamma$ , which we fit to each of the four data sets in Figure 3. The fits are shown in Figure 3 and the resulting parameter values are collected in Table 1. The table also includes the apparent (temperature-dependent) Arrhenius activation energy,  $E_A \equiv -k_B T^2(d \ln \tau_R/dT) = \gamma k_B T^2/(T - T_0)$ , at two



**Table 1. Results from Fits to Temperature-Dependent Trehalose  $^2\text{H}$   $R_1$ <sup>a</sup>**

property	249.3 mM	199.4 mM	99.7 mM	49.8 mM <sup>b</sup>	$\eta_0/T$ <sup>c</sup>
$(\omega_Q S)^2$ ( $10^{11} \text{ s}^{-2}$ )	3.55(2)	3.56(2)	3.57(2)	3.57(8)	
$\tau_R^0$ (ps)	12.3(4)	11.8(4)	10.4(3)	10.4(1.5)	
$T_0$ (K)	208(2)	211(2)	211(2)	222(7)	218(1)
$\gamma$	2.7(1)	2.6(1)	2.6(1)	2.2(3)	2.14(2)
$\chi_{\text{red}}^2$	0.41	0.77	0.35	0.36	1.04
$E_A^{290}$ (kJ mol <sup>-1</sup> ) <sup>d</sup>	24(1)	23(1)	23(1)	22(4)	20.7(3)
$E_A^{240}$ (kJ mol <sup>-1</sup> ) <sup>d</sup>	42(4)	44(4)	44(4)		46(1)

<sup>a</sup>Uncertainty (one standard deviation) in the last digit given within parentheses. <sup>b</sup>Fit based on data in the temperature range 243.1–293.2 K. <sup>c</sup>From power-law fit to  $\eta_0/T$  for bulk  $\text{H}_2\text{O}$  in temperature range 249.2–293.2 K. <sup>d</sup>Apparent activation energy at 240 and 290 K.

temperatures. As the solution is diluted, the parameters gradually approach the corresponding values for  $\eta_0/T$ , as expected from the Stokes–Einstein–Debye (SED) relation:

$$\tau_R = \frac{\eta_0 V_{\text{hyd}}}{k_B T} \quad (2)$$

where  $V_{\text{hyd}}$  is the hydrodynamic volume of the solute. As we shall show (see Secondary Dynamic Solvent Effect), the deviation, at finite trehalose concentration, of the temperature dependence of  $\tau_R$  from that predicted by eq 2 is caused by the slowing down of water motions in the hydration layer.

The excellent fit quality evident in Figure 3 and Table 1 shows that the temperature dependence of  $\tau_R$  is accurately described by a fractional power law, as is the case for all transport properties of the  $\text{H}_2\text{O}$  solvent.<sup>59</sup> However, the power-law function should be viewed as an interpolation device rather than as a physical model. Given that  $\tau_R$  is the only temperature-dependent parameter, it follows from eq 1 that  $\tau_R(T_{\text{max}}) = 0.6158/\omega_0$  and that  $R_1(T_{\text{max}}) = 0.2850(\omega_Q S)^2/\omega_0$  at the (slightly concentration-dependent) temperature  $T_{\text{max}}$  of the  $R_1$  maximum. We can therefore obtain the parameter  $(\omega_Q S)^2$  from the  $R_1$  maximum, determined by using the fractional power law as an interpolation function. Once the  $(\omega_Q S)^2$  value has been determined, we can obtain  $\tau_R$  by numerically inverting eq 1, without recourse to the power-law parametrization. The  $\tau_R$  values obtained in this way (Figure 4) are virtually identical to the ones obtained from a direct fit based on the power-law parametrization.

The nuclear quadrupole frequency  $\omega_Q = (3/2)^{1/2} \pi \chi(1 + \eta^2/3)^{1/2}$  is related to the quadrupole coupling constant  $\chi$  and the asymmetry parameter  $\eta$  of the electric field gradient tensor. From a comparison of  $^2\text{H}$  and  $^{13}\text{C}$  relaxation rates,  $\chi = 178.6$  kHz was determined for the HC2 and HC3 positions in  $\alpha$ -D-glucose.<sup>48</sup> Adopting this value and setting  $\eta = 0$  (because  $\eta \ll 1$  for  $^2\text{H}$  in C–D bonds), we obtain  $\omega_Q = 6.87 \times 10^5 \text{ rad s}^{-1}$ . Combining this with the average of the  $(\omega_Q S)^2$  values in Table 1, we obtain  $S^2 = 0.754 \pm 0.004$ . Except for D/H isotope effects, the  $^2\text{H}$  order parameter for a carbon-bound deuteron should be identical to the  $^{13}\text{C}$  order parameter for the corresponding C–H bond. The average  $^2\text{H}$  order parameter of 0.75 found here for trehalose is somewhat smaller than the  $^{13}\text{C}$  order parameters reported for the glucose moiety of sucrose<sup>51–54</sup> and for trehalose<sup>25</sup> (at <300 K):  $0.85 \pm 0.05$  for the ring carbons and  $0.75 \pm 0.05$  for the hydroxymethyl carbon.

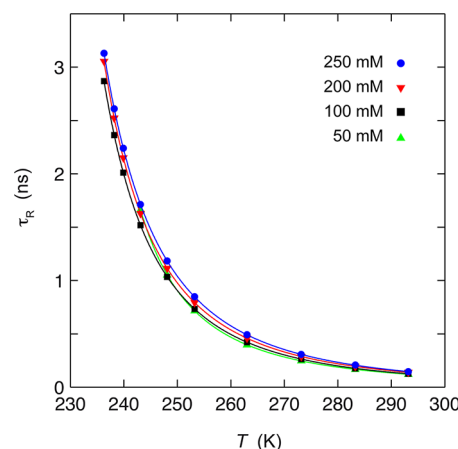


**Figure 4.** Trehalose tumbling time  $\tau_R$  versus temperature in aqueous solutions at four trehalose concentrations. Error bars are smaller than the symbol size, except at 50 mM.

**Trehalose–Trehalose Interactions.** From the fit results in Table 1 or from the invariance of the maximum  $R_1$  in Figure 3, we conclude that  $S^2$  does not depend significantly on trehalose concentration up to 0.25 M. In the following, we assume that this is true for all concentrations up to 1.47 M. The  $R_1$  data in Figure 2 can then be converted to  $\tau_R$  by setting  $(\omega_Q S)^2 = 3.56 \times 10^{11} \text{ s}^{-2}$  and inverting eq 1.

As seen from Figure 5,  $\tau_R$  increases monotonically with increasing concentration  $C$  over the entire range examined here

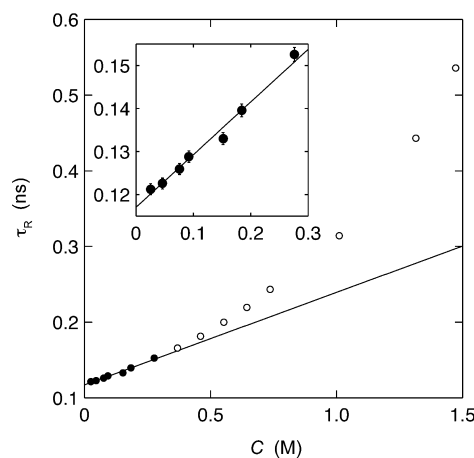


**Figure 5.** Trehalose tumbling time  $\tau_R$  versus concentration in aqueous solution at 293.2 K. The inset magnifies the dilute regime. The line was fitted to the data below 0.3 M (solid symbols).

(0.025–1.47 M). The increase of  $\tau_R$  is linear below  $\sim 0.3$  M, but at higher concentrations  $\tau_R$  increases faster. A linear fit in the dilute regime ( $<0.3$  M) yields  $\tau_R(0) = 0.117 \pm 0.001 \text{ ns}$ ,  $\partial\tau_R/\partial C = 0.122 \pm 0.007 \text{ ns M}^{-1}$  and a linear correlation coefficient  $r = 0.992$ . Inserting  $\tau_R(0)$  and  $\eta_0 = 1.002 \text{ cP}$  (the viscosity of  $\text{H}_2\text{O}$  at 293.2 K) into eq 2, we obtain for the hydrodynamic volume  $V_{\text{hyd}} = 473 \pm 4 \text{ \AA}^3$ . This is nearly 40% larger than the (apparent) partial molecular volume of trehalose,  $V_T = 343.5 \text{ \AA}^3$ , at 293.2 K and infinite dilution,<sup>60</sup> a difference that we attribute partly to the surface roughness and nonspherical shape of the trehalose molecule (Figure 1) and partly to a second-order dynamic hydration effect (see below). The former effect may be estimated by using atomic-level hydrodynamics<sup>55</sup> to

compute  $\tau_R(0)$  from the crystal structure of trehalose (PDB ID 1j1m) and then using eq 2 to deduce an effective hydrodynamic volume. The effective atomic radius used in the calculation was set to 1.8 Å, estimated<sup>61</sup> by taking the average of the primary peak positions in the  $O_W-O$  and  $O_W-C$  pair correlation functions (2.8 Å and 3.6 Å, respectively<sup>36,38,39,62</sup>) and subtracting 1.4 Å (the van der Waals radius of  $H_2O$ ). In this way, we obtain 460 Å<sup>3</sup>, not far from the value (473 Å<sup>3</sup>) deduced from the intercept in Figure 5.

Two distinct physical mechanisms can contribute to the concentration dependence of  $\tau_R$ : hydrodynamic “interactions” and mechanical interactions. The effect of hydrodynamic interactions can be estimated from continuum mechanics,<sup>63</sup> according to which the single-particle tumbling time for a suspension of hard spheres increases with the volume fraction  $\phi$  as  $\tau_R(\phi) = \tau_R(0) [1 + 0.67\phi + O(\phi^2)]$ . With  $\phi = CV_T$  and  $\tau_R(0)$  from the intercept in Figure 5, we obtain  $\partial\tau_R/\partial C = 0.016$  ns M<sup>-1</sup>, an order of magnitude less than the observed initial slope. We therefore conclude that the concentration dependence of  $\tau_R$  is caused by mechanical (direct or solvent-mediated) interactions among the trehalose molecules.

To understand the nature of these interactions, it is helpful to estimate the typical separation  $L$  between trehalose molecules in a solution of molar concentration  $C$ . If the trehalose molecules, with effective diameter  $\sigma = (6V_T/\pi)^{1/3} \approx 9$  Å, are placed on a uniformly expanded cubic lattice, then the center-to-center distance  $D$  is given by  $D = \sigma(\phi_0/\phi)^{1/3}$ , where  $\phi = CV_T$  and  $\phi_0 = 0.7405$  is the volume fraction for cubic close packing. Hence,  $L = D - \sigma = \sigma[1.53(C/M)^{-1/3} - 1]$ . For  $C = 0.1$  M, where trehalose–trehalose interactions are already manifested (Figure 5), we thus have  $L \approx 21$  Å, or  $\sim 7$  water layers. Because (neutral) trehalose molecules do not interact significantly over such long distances, we conclude that trehalose clustering occurs even at the comparatively low concentration of 0.1 M. At our highest concentration,  $C = 1.47$  M, a similar estimate yields  $L \approx 3$  Å or one water layer, so direct interactions should be significant even in the absence of clustering.

Rather than attempting to model the structures, populations and dynamics of trehalose clusters,<sup>42</sup> we adopt a semi-phenomenological approach where we reinterpret the parameters of the SED relation as effective quantities that may depend on temperature as well as on concentration. Specifically, we consider two limiting scenarios described by eq 2 with (I) an effective hydrodynamic volume  $V_{\text{hyd}}^{\text{eff}}(T, C)$  and the bulk solvent viscosity  $\eta_0(T)$ , or with (II) an effective viscosity  $\eta_{\text{eff}}(T, C)$  and the (constant) infinite-dilution hydrodynamic volume  $V_{\text{hyd}}$ . Scenario I is more appropriate if the solution contains well-defined trehalose aggregates (oligomers) with a lifetime that is long compared to their tumbling time. Scenario II should be a better description if the trehalose–trehalose interactions are transient. The effective viscosity  $\eta_{\text{eff}}(T, C)$  may then be more closely related to the macroscopic solution viscosity  $\eta(T, C)$  than to the solvent viscosity  $\eta_0(T)$ .

In their molecular dynamics simulation study of 0.2–1.8 M trehalose solutions at 298 K, Sapir and Harries found trehalose clusters with a broad size distribution at all examined concentrations.<sup>42</sup> The clusters were found to exchange monomers on a time scale of  $\sim 10$  ps and to break up on a time scale of a few 100 ps.<sup>42</sup> Because our tumbling times (at 293 K) are in the range 0.1–0.5 ns (Figure 5), scenario II appears to be the more relevant one. We thus calculate an effective viscosity  $\eta_{\text{eff}}(C)$  from eq 2, using the experimental  $\tau_R$

values measured at 293.2 K (Figure 5) and the fixed (infinite-dilution) hydrodynamic volume,  $V_{\text{hyd}} = 473$  Å<sup>3</sup>, obtained by combining eq 2 with the intercept in Figure 5. The effective viscosity  $\eta_{\text{eff}}(C)$  deduced in this way closely follows the macroscopic solution viscosity  $\eta(C)$ , measured with a capillary viscometer at 293.2 K,<sup>64</sup> up to  $\sim 0.75$  M (Figure 6). But at

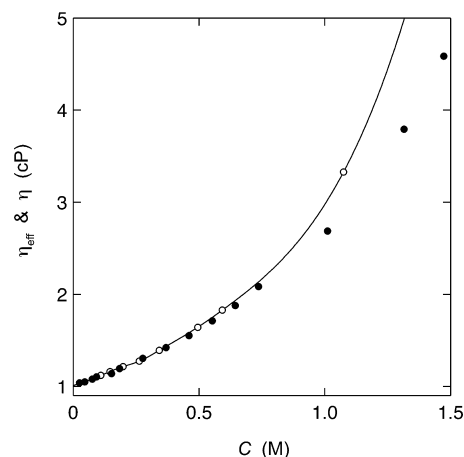


**Figure 6.** Effective viscosity  $\eta_{\text{eff}}$  derived from the tumbling time  $\tau_R$  (solid symbols) and macroscopic solution viscosity<sup>64</sup>  $\eta$  (open symbols) versus trehalose concentration in aqueous solution at 293.2 K. The curve, intended as a visual guide, is the cubic spline interpolant of the macroscopic viscosity data.

higher concentrations the macroscopic viscosity increases more strongly with  $C$ . Above the percolation threshold, located at 1.1–1.5 M in the MD simulation study,<sup>42</sup> the macroscopic viscosity is expected to rise dramatically, but because the trehalose–trehalose interactions are transient,<sup>42</sup> the tumbling of individual trehalose molecules is not slowed down to the same extent. Such a view is consistent with our results.

If the solution contained a concentration-dependent distribution of long-lived trehalose oligomers (scenario I), then eq 1 would have to be replaced by a sum (or integral) over oligomer species with different tumbling times. At low temperatures, where  $\omega_0\tau_R \gtrsim 1$ , such a scenario could be identified from the frequency dependence of  $R_1$ . Although we have not recorded such magnetic relaxation dispersion data, we note that the observed concentration-independent maximum  $R_1$  (Figure 3) is predicted by eq 1 with a single tumbling time  $\tau_R$ . It is therefore not, in general, consistent with scenario I. We note also that, though a monomer–dimer equilibrium can account for the initial linear increase of  $\tau_R(C)$  (with an association constant of 0.5 M<sup>-1</sup> if  $\tau_{R2} = 2\tau_{R1}$ ), it cannot explain the positive curvature of  $\tau_R(C)$  at higher concentrations (Figure 5).

**Trehalose Hydration Dynamics.** To avoid contributions from the labile hydroxyl hydrogens in trehalose,<sup>24</sup> water dynamics was studied via the <sup>17</sup>O relaxation rate  $R_1$  of <sup>17</sup>O-enriched water in the same samples that were used for trehalose <sup>2</sup>H relaxation measurements. We consider first the concentration dependence of  $R_1$  at 293 K (Figure 7).

In contrast to trehalose, water molecules tumble so fast, even at 236 K, that  $R_1$  is independent of the Larmor frequency  $\omega_0$  (the so-called extreme motional narrowing limit<sup>47</sup>). As a consequence,  $R_1$  is proportional to the integral correlation time  $\tau$ , defined as the integral of the normalized electric field gradient time correlation function.<sup>59</sup> The correlation time  $\tau$  is

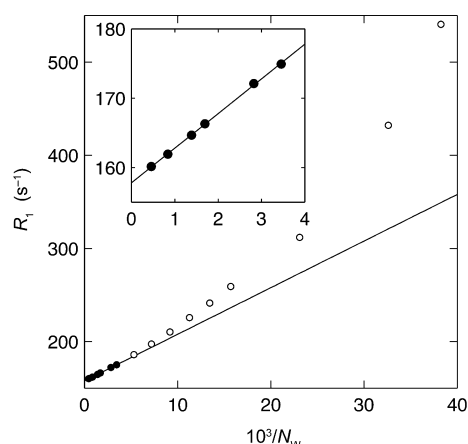


**Figure 7.** Water  $^{17}\text{O}$  relaxation rate  $R_1$  versus trehalose concentration, expressed in terms of the water/trehalose mole ratio  $N_W$ , in aqueous solution at 293.2 K. The inset magnifies the dilute regime. Error bars are smaller than or comparable to the symbol size. The line was fitted to the data with  $1/N_W < 0.004$  or  $C < 0.2$  M (solid symbols).

proportional to the mean waiting time between successive large-angle jumps, where the water molecule switches H-bond partners.<sup>59,65</sup> Moreover,  $\tau$  is averaged over all local environments in the solution, which may differ substantially in H-bond exchange rate. At sufficiently low trehalose concentration, individual trehalose molecules should contribute independently to  $R_1$  by perturbing water dynamics in their immediate surroundings. It is not obvious that this “independent hydration limit” is applicable to our data, because solute–solute interactions slow down trehalose tumbling even at the lowest concentrations examined (Figure 5). Judging from MD simulations,<sup>42</sup> the trehalose clusters are sparse (rather than compact) so direct trehalose–trehalose interactions typically involve only a small part of the molecule (often just a single solute–solute H-bond) and only a minor fraction of the trehalose molecules is involved in clusters at low concentrations. Under such conditions, the independent hydration limit is likely to remain a good approximation.

In the independent hydration regime, the water  $^{17}\text{O}$  relaxation rate may be expressed as<sup>45</sup>

$$R_1 = R_1^0 \left( 1 + \frac{\nu_{\text{dyn}}}{N_W} \right) \quad (3)$$

where  $N_W$  is the overall water/trehalose mole ratio in the solution (Supporting Information S3) and  $R_1^0$  is the relaxation rate of bulk water, unaffected by the solute. The solute-induced perturbation of water dynamics is captured by the dynamic hydration number,

$$\nu_{\text{dyn}} = \nu_H(\xi - 1) \quad (4)$$

which involves the static (geometric) hydration number  $\nu_H$ , here defined as the number of water molecules in the first hydration shell, and the dynamic perturbation factor (DPF)

$$\xi = \frac{\langle \tau_H \rangle}{\tau_0} \quad (5)$$

Here,  $\tau_0$  is the correlation time in bulk water and  $\langle \tau_H \rangle$  is the average correlation time for the  $\nu_H$  perturbed water molecules. The DPF is thus a measure of the relative slowing down of

water rotation (and H-bond exchange) of these  $\nu_H$  water molecules.

The  $R_1$  data are linear up to  $C \approx 0.25$  M (or  $N_W \approx 200$ ), but at higher concentrations the dynamic perturbation increasingly exceeds the linear prediction of eq 3 (Figure 7). From the fit in the linear regime (Figure 7), we obtain  $R_1^0 = 157.8 \pm 1.3 \text{ s}^{-1}$  (consistent with the value  $158.6 \text{ s}^{-1}$  measured on a bulk water reference sample) and  $\nu_{\text{dyn}} = 31.5 \pm 0.8$ . Without further assumptions, we cannot separate  $\nu_{\text{dyn}}$  into its constituent factors, related to the range ( $\nu_H$ ) and magnitude ( $\xi$ ) of the dynamic perturbation. In particular, it is not possible to identify  $\nu_H$  with the  $N_W$  value ( $\sim 200$ ) where the linearity breaks down, because the change of slope may simply reflect concentration-dependent self-association of trehalose.<sup>42</sup> However, previous spin relaxation<sup>45</sup> and MD simulation<sup>66–68</sup> studies of a variety of organic solutes indicate that the dynamic perturbation of the solvent is essentially confined to the water molecules in direct contact with the solute, that is, to the first hydration layer. We assume that this is the case also for trehalose.

MD simulations have shown that the number of water molecules in the first hydration layer of organic solutes (and proteins) can be accurately estimated by computing the solvent-accessible surface area  $A_S$  (with  $1.7 \text{ \AA}$  probe radius) and dividing by  $10.75 \text{ \AA}^2$  (the mean surface area per water molecule).<sup>45</sup> Using GetArea<sup>69</sup> to compute  $A_S$  from the crystal structure, we obtain  $\nu_H = 47.2$  for trehalose dihydrate<sup>50</sup> and  $\nu_H = 46.4$  for trehalose bound to the protein ricin (PDB code 1j1m). With  $\nu_H = 47$ , eq 4 yields  $\xi = 1.67 \pm 0.02$  for the average DPF in the first hydration layer of trehalose at 293 K. This value falls in the range 1–2 of all previously determined DPFs (with  $\nu_H$  computed in the same way as here) for small organic solutes at room temperature.<sup>45</sup> Extrapolating to 298 K (see below), at which temperature DPF values have been quoted previously,<sup>45</sup> we obtain  $\xi = 1.60 \pm 0.02$  for trehalose. Within experimental accuracy, trehalose has the same DPF as, for example, *n*-propanol, 1,5-pentanediol, and tetramethylurea.<sup>45</sup>

Uedaira et al. reported water  $^{17}\text{O}$   $R_1$  data at 67.8 MHz from aqueous solutions of four disaccharides at 298 K: sucrose, maltose, melibiose, and trehalose.<sup>23,70</sup> All their data were acquired at concentrations above those used here to establish the linear regime for trehalose. They fitted  $R_1$  to a quadratic polynomial in  $1/N_W$  and extracted  $\nu_{\text{dyn}}$  from the linear coefficient. Computing  $\nu_H$  as described above for trehalose from available crystal structures of these disaccharides (PDB code 1ylj for sucrose, 2bhz for maltose, and 1ugy for melibiose), we obtain  $\nu_H = 45.0$ ,  $46.1$ , and  $48.2$ , respectively. Combining this with the  $\nu_{\text{dyn}}$  values reported by Uedaira et al.,<sup>23,70</sup> we obtain  $\xi = 1.56$ ,  $1.59$ , and  $1.56$ , respectively, and  $1.54$  for trehalose. Considering the high concentrations used and the lower  $R_1$  accuracy (mainly due to the use of water with the natural 0.037 atom %  $^{17}\text{O}$  abundance), these data do not establish any significant difference in the perturbation of water dynamics among the four investigated disaccharides. In fact, also the difference between our result ( $\xi = 1.60 \pm 0.02$ ) and theirs ( $\xi = 1.54$  with unknown, but larger, error) for trehalose is probably not significant. For completeness we mention a subsequent natural-abundance  $^{17}\text{O}$  relaxation study (at 36.6 MHz) of sucrose, maltose, and trehalose solutions (at 303 K) at even higher concentrations and with even larger data scatter.<sup>71</sup> The results deduced from these data are therefore questionable. For example, the  $\nu_{\text{dyn}}$  value obtained at 303 K for trehalose is a factor 1.9 larger than that reported by Uedaira et al.<sup>23</sup> at 298 K (and this cannot be explained by the slight temperature



difference, because, in this range,  $\nu_{\text{dyn}}$  decreases with increasing temperature; see below).

**Temperature-Dependent Hydration Dynamics.** To study the temperature dependence of water rotation in the hydration layer, we measured the  $^{17}\text{O}$  relaxation rate at several concentrations in the independent hydration regime ( $C \leq 0.25$  M) and at 10 temperatures from 293 K down to 236 K, close to the practical limit of supercooling in emulsions. As at 293 K (Figure 7),  $R_1$  was found to increase linearly with trehalose concentration ( $1/N_{\text{W}}$ ) at all temperatures (Figure S7, Supporting Information). From the slope of the linear fits (Figure S7, Supporting Information), we obtained the dynamic hydration number  $\nu_{\text{dyn}}$  according to eq 3. Setting  $\nu_{\text{H}} = 47$  (see above), we then obtained the DPF  $\xi$  from eq 4. The result at 293 K,  $\xi = 1.67 \pm 0.02$ , is identical to the one derived from measurements on nonemulsified samples (Figure 7 inset). Upon cooling, the DPF first increases, passes through a broad maximum at 260.1 K (where  $\xi = 1.93$ ), and then drops sharply (Figure 8). Below the practically unattainable temperature of 234 K, our results indicate that  $\xi < 1$ , that is, hydration water rotates faster than bulk water.

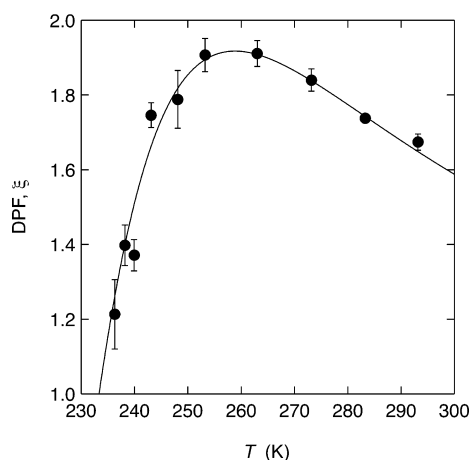


**Figure 8.** Temperature dependence of the dynamic perturbation factor  $\xi$  for trehalose, determined from  $^{17}\text{O}$   $R_1$  data in the independent hydration regime. The curve was obtained by fitting  $\tau_0(T)$  to a fractional power law and  $\langle\tau_{\text{H}}(T)\rangle = \xi \tau_0$  to a three-parameter rational fraction and using eq 5.

The bulk water correlation time  $\tau_0$  has a strong temperature dependence, which, in the supercooled regime, deviates strongly from the Arrhenius law.<sup>59</sup> As a result, the apparent activation energy,  $E_{\text{A}}^0 \equiv -k_{\text{B}}T^2 \text{d} \ln \tau_0 / \text{d}T$ , increases strongly on cooling. This behavior is believed to be a consequence of the gradual approach to perfect tetrahedral coordination as the liquid is cooled.<sup>59</sup> In contrast, the average correlation time  $\langle\tau_{\text{H}}\rangle$  in the hydration layer does not deviate much from Arrhenius behavior (Figure S8, Supporting Information) and the associated apparent activation energy  $E_{\text{A}}^{\text{H}} \equiv -k_{\text{B}}T^2 \text{d} \ln \langle\tau_{\text{H}}\rangle / \text{d}T$  only increases weakly on cooling (Figure S9, Supporting Information). At room temperature  $E_{\text{A}}^{\text{H}}$  is a few  $\text{kJ mol}^{-1}$  higher than  $E_{\text{A}}^0$ , at 260 K  $E_{\text{A}}^{\text{H}} = E_{\text{A}}^0$  (at the  $\xi$  maximum in Figure 8), and at still lower temperatures  $E_{\text{A}}^{\text{H}} < E_{\text{A}}^0$  (Figure S9, Supporting Information). The reason that  $\langle\tau_{\text{H}}\rangle$  has a weaker temperature dependence than  $\tau_0$  below 260 K is that the H-bond coordination changes less in the hydration layer than in bulk water because the solute structure is essentially temperature-independent.<sup>45</sup>

**Secondary Dynamic Solvent Effect.** In a solution, the dynamics of solute and solvent are necessarily coupled by their mutual intermolecular interactions. As demonstrated above, the trehalose solute induces only a moderate slowing down of water rotation (and H-bond exchange) in the hydration layer. In contrast, solute dynamics are coupled to solvent dynamics to first order (not merely as a perturbation), as expressed by the proportionality between solute tumbling time  $\tau_{\text{R}}$  and solvent viscosity  $\eta_0$  in the SED relation, eq 2. The dynamical coupling is so strong that we can identify a second-order effect, where the solute's perturbation of solvent dynamics reacts back on the solute and alters  $\tau_{\text{R}}$ . In a sense, this back-reaction is an artifact of describing a strongly interacting system (solute + solvent) in terms of two subsystems. Nevertheless, it is a useful description.

In the literature, this secondary dynamic solvent effect on  $\tau_{\text{R}}$  is often described in terms of an “iceberg” model, where “bound” water molecules increase the effective hydrodynamic volume of the solute.<sup>72</sup> But, as we have seen, the hydration waters are highly mobile. For example, at 293 K,  $\tau_0 = 1.9$  ps, and  $\langle\tau_{\text{H}}\rangle = 1.67 \times 1.9 = 3.2$  ps, so we expect the average residence time of water molecules in the hydration layer to be of order 10 ps. This is an order of magnitude less than the tumbling time,  $\tau_{\text{R}} = 117$  ps, of trehalose at infinite dilution (Figure 5). Because a typical hydration water molecule is exchanged several times before the solute has randomized its orientation, the “iceberg” model is inappropriate.

A better, albeit still approximate, model is to allow the solvent viscosity in the SED relation to vary with the distance from the solute. Specifically, we assume that the solvent viscosity is  $\eta_{\text{H}}$  in the hydration layer and that it assumes the bulk water value  $\eta_0$  outside this layer. Furthermore, we assume that  $\eta_{\text{H}}/\eta_0 = \langle\tau_{\text{H}}\rangle/\tau_0 \equiv \xi$ . (This identification is supported by the observation that  $\tau_0$  obeys eq 2 to high accuracy even in the supercooled regime.<sup>59</sup>) We can then use the DPF derived from the  $^{17}\text{O}$  relaxation data to describe the secondary dynamic solvent effect on  $\tau_{\text{R}}$ .

By solving the linearized Navier–Stokes equations for the local viscosity model, one finds that the SED relation, eq 2, remains valid provided that the bulk solvent viscosity  $\eta_0$  is replaced by an effective solvent viscosity  $\eta_{\text{eff}}^0$  given by<sup>61</sup>

$$\frac{1}{\eta_{\text{eff}}^0} = \frac{\alpha}{\eta_0} + \frac{(1-\alpha)}{\eta_{\text{H}}} = \frac{1}{\eta_0} \left[ \alpha + \frac{(1-\alpha)}{\xi} \right] \quad (6)$$

Here  $\alpha \equiv V_{\text{T}}/(V_{\text{T}} + V_{\text{H}})$ , where  $V_{\text{T}}$  is the volume of the trehalose solute and  $V_{\text{H}}$  is the volume of the hydration layer. We use the partial volume,  $V_{\text{T}} = 343.5 \text{ \AA}^3$ , of trehalose at 293 K.<sup>60</sup> With the hydration number  $\nu_{\text{H}} = 47$  (see above) and the molecular volume,  $V_{\text{W}} = 30.0 \text{ \AA}^3$ , of  $\text{H}_2\text{O}$  at 293 K, we obtain  $V_{\text{H}} = \nu_{\text{H}}V_{\text{W}} = 1410 \text{ \AA}^3$  and  $\alpha = 0.196$ .

Note that  $\eta_{\text{eff}}^0$  is still a *solvent* viscosity. It may be identified with the  $C \rightarrow 0$  limit of the effective *solution* viscosity  $\eta_{\text{eff}}(C)$  introduced to describe the increase of  $\tau_{\text{R}}$  with trehalose concentration (see above). It is instructive to consider the limits of eq 6. In the absence of solvent perturbation ( $\xi = 1$  or  $\nu_{\text{H}} = 0$ ), eq 6 yields  $\eta_{\text{eff}}^0 = \eta_0$  as expected. In the limit of strong dynamic perturbation, in the sense that  $\xi \gg V_{\text{H}}/V_{\text{T}}$  ( $V_{\text{H}}/V_{\text{T}} \approx 4$  here), eq 6 yields  $\eta_{\text{eff}}^0 = \eta_0/\alpha$ . When this is inserted into eq 2, we obtain the ideal SED relation with bulk solvent viscosity  $\eta_0$  but with an augmented hydrodynamic volume  $V_{\text{hyd}} = V_{\text{T}} + V_{\text{H}}$ , as in the iceberg model.

To test the local viscosity model, we consider the second-order temperature dependence of  $\tau_{\text{R}}$  that remains after the first-

order temperature dependence (from the solvent viscosity  $\eta_0$ ) has been removed by dividing  $\tau_R$  by  $\tau_R^0$ . With the limiting tumbling time  $\tau_R^0$  given by eq 2 with  $V_{\text{hyd}} = V_T$ , we obtain

$$\frac{\tau_R}{\tau_R^0} = \frac{\tau_R(T)k_B T}{\eta_0(T)V_T} \quad (7a)$$

Figure 9 shows the temperature dependence of the ratio  $\tau_R/\tau_R^0$  calculated from eq 7a using the  $^2\text{H}$ -derived trehalose

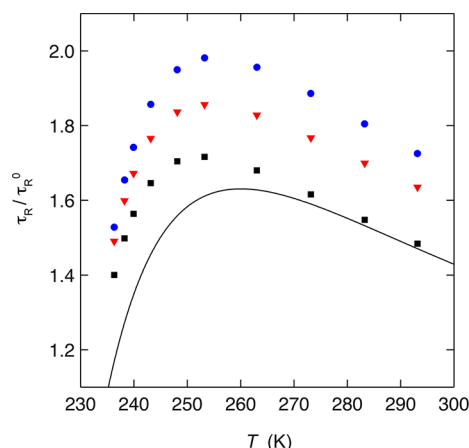


**Figure 9.** Trehalose tumbling time  $\tau_R$  obtained from the  $^2\text{H}$   $R_1$  data and normalized by the SED limit  $\tau_R^0$  versus temperature in aqueous trehalose solutions at  $C = 100$  mM (black squares), 200 mM (red triangles), and 250 mM (blue circles). The curve is the ratio  $\tau_R/\tau_R^0$  obtained from the water  $^{17}\text{O}$   $R_1$  data according to eq 7b.

tumbling time  $\tau_R$  (Figure 4) at three trehalose concentrations (all in the independent hydration regime; the 50 mM data were not included here due to their limited temperature range and larger experimental error) and the bulk water viscosity  $\eta_0$ . (The viscosity of bulk  $\text{H}_2\text{O}$  has been reliably measured only down to 253 K;<sup>57</sup> for lower temperatures we use an empirical formulation.<sup>58</sup>) Apart from the linear increase of  $\tau_R$  with concentration, already discussed in connection with Figure 5, the salient feature of the data in Figure 9 is the maximum near 255 K seen at all three concentrations.

At first sight, one might be tempted to attribute this maximum to temperature-dependent trehalose clustering. But the striking resemblance between the maxima in Figures 8 and 9 suggests another explanation. According to the local viscosity model, also  $\tau_R$  is given by eq 2 provided that the bulk solvent viscosity  $\eta_0$  is replaced by an effective solvent viscosity  $\eta_{\text{eff}}^0$ . Combining eqs 2 and 6, we thus obtain

$$\frac{\tau_R}{\tau_R^0} = \left[ \alpha + \frac{(1 - \alpha)}{\xi(T)} \right]^{-1} \quad (7b)$$

With the aid of eq 7b and  $\alpha = 0.196$  (see above), we can calculate the temperature-dependent ratio  $\tau_R/\tau_R^0$  from the  $^{17}\text{O}$ -derived DPF  $\xi(T)$  (Figure 8). The resulting curve in Figure 9 shows a maximum similar to the one deduced from the measured trehalose tumbling time, albeit shifted by  $\sim 5$  K.

One could argue that the hydrodynamic volume to be used in eqs 7a and 7b (via  $\alpha$ ) should be somewhat larger than the partial volume  $V_T$  to take into account effects on  $\tau_R$  of surface roughness and nonspherical molecular shape. Increasing  $V_T$  in eq 7a reduces  $\tau_R/\tau_R^0$  but does not alter the temperature dependence of the three profiles in Figure 9. Increasing  $V_T$  in

eq 7b also reduces  $\tau_R/\tau_R^0$  (but less so than in eq 7a, thus bringing the curve into closer agreement with the data symbols in Figure 9) and has an insignificant effect on the temperature dependence of the curve in Figure 9. In principle, the maximum in  $\tau_R/\tau_R^0$  could be caused by a nonmonotonic variation in the conformation of trehalose, in particular, the glycosidic dihedral angles. If such changes occurred, they would be reflected in the partial volume  $V_T$ . But measurements in the range 263–293 K show that  $V_T$  increases (linearly) with temperature (by 5% at infinite dilution and by 4% at 1.5 M),<sup>73</sup> the opposite of what is required to explain the decrease of  $\tau_R/\tau_R^0$  in this temperature range (Figure 9).

In conclusion, it seems clear that the maximum in  $\tau_R/\tau_R^0$  is caused by a secondary dynamic solvent effect, where the solute slows down its own motion by interfering with H-bond exchange in the hydration layer. To our knowledge, this effect has not been directly demonstrated before. The same effect has previously been invoked to reconcile experimental tumbling times of globular proteins with the  $\tau_R^0$  values computed with molecular hydrodynamics and with the DPF for the protein hydration layer.<sup>61</sup> However, in that case, the temperature dependence was not considered.

**Concentrated Regime.** The linear dependence of the water  $^{17}\text{O}$   $R_1$  on  $1/N_W$  up to  $C \approx 0.25$  M (Figure 7) establishes the range of the independent hydration regime, where eq 3 applies. Any interpretation of the further increase of  $R_1$  at higher concentrations (Figure 7) is strongly model-dependent even in the absence of trehalose clustering.

If trehalose–trehalose interactions are sufficiently repulsive, we can use the expanded cubic lattice model (see above) to estimate an overlap concentration  $C^* \approx 0.77$  M (or  $N_W^* \approx 60$ ) where the center-to-center separation exceeds the trehalose diameter (9 Å) by 2 water diameters ( $2 \times 3$  Å). Beyond this concentration, if not before, we expect the dynamic hydration number in eq 3 to depend on concentration:  $\nu_{\text{dyn}}(C) = \nu_H(C)[\xi(C) - 1]$ . As indicated, both factors in  $\nu_{\text{dyn}}$  may show a concentration dependence:  $\nu_H(C)$  should decrease when the hydration layers of adjacent solute molecules overlap (at  $C > C^*$ ), whereas the DPF  $\xi(C)$  is likely to increase when water molecules are confined by, and interact with, two or more solute molecules. (Analogous intramolecular confinement effects dominate the average DPF in the heterogeneous hydration layer of proteins.<sup>74</sup>) The strong nonlinear increase of  $R_1$  at  $C > C^*$  suggests that the confinement effect dominates at these concentrations. Indeed, for  $N_W < \nu_H(0) = 47$  (or  $C > 0.94$  M), all water molecules are directly coordinated to trehalose molecules and eq 3 should be replaced by  $R_1(C) = R_1^0 \xi(C)$ .

The interpretation of  $^{17}\text{O}$  relaxation data outside the independent hydration regime is further complicated by trehalose clustering, as indicated by the concentration dependence of the trehalose tumbling time (Figure 5) and by MD simulations where  $\sim 25\%$  of the trehalose molecules make at least one H-bond with another trehalose molecule already at  $C = 0.2$  M.<sup>42</sup> It might be tempting to identify a breakpoint between two linear regimes in Figure 7 at  $N_W \approx 167$  (or  $C \approx 0.31$  M). If this apparent breakpoint were interpreted as an overlap concentration (where  $N_W = \nu_H$ ), then the perturbed hydration region would include two water layers, rather than one layer as we have assumed, and the increase in slope at the breakpoint would imply a large increase of the DPF. But the concentration dependence of the trehalose tumbling time (Figure 5) suggests a more plausible interpretation, where the



first increase of the slope  $\partial R_1/\partial C$  around 0.25 M occurs, not because there is no longer any bulk (unperturbed) water in the solution, but because trehalose clustering gives rise to a minor population (that increases with  $C$ ) of confined and more strongly perturbed water. In conclusion, our data are consistent with a short-ranged solvent perturbation, where only water molecules in direct contact with trehalose differ significantly from bulk water. Furthermore, the dynamic perturbation factor determined in the independent hydration regime (where the effect of trehalose aggregation is insignificant) falls in the same range as for most other small organic solutes.<sup>45</sup>

**Comparison with Terahertz Spectroscopy.** Measuring the dielectric absorption of aqueous trehalose solutions in the frequency window 2.1–2.8 THz and interpreting the results with the same two-state hydration model as we have used here, Heyden et al. concluded that the dynamic perturbation of the solvent extends to two water layers.<sup>26</sup> These measurements probe collective vibrations on the 100 fs time scale in the intact H-bond network of water, whereas  $^{17}\text{O}$  relaxation monitors single-molecule rotation enabled by the restructuring of this network on a time scale of several picoseconds. Because different length and time scales are involved, vibrational and structural dynamics may be perturbed to different extents by the solute. However, as explained below, we do not believe that the data of Heyden et al. can be used to determine the range of the terahertz perturbation.

The dielectric absorption coefficient  $\alpha(C)$  is related to the spectral density of the total electric dipole moment of the sample. Therefore,  $\alpha(C)$  has contributions from solute, bulk water, and hydration water as well as from cross-correlations between these components.<sup>75</sup> If the cross-correlations are neglected (although it is unclear if this is justified), one obtains for the two-state hydration model<sup>26</sup>

$$\alpha(C) = \alpha_0[1 + CV_W(\nu_{\text{dyn}}^{\text{THz}} + \delta_T)] \quad (8)$$

where  $\alpha_0$  is the absorption coefficient of bulk water. Equation 8 differs in two ways from the analogous eq 3. First, because  $\alpha$  is a volume-based average whereas  $R_1$  is a molecular average, eq 8 contains  $CV_W$  instead of  $1/N_W$  (the difference is small at low concentrations, for example, 4% at 0.2 M). Second, because  $\alpha$  has contributions from all dipoles whereas  $R_1$  only monitors water molecules, eq 8 contains a (dominant) term  $\delta_T = (V_T/V_W)(\alpha_T/\alpha_0 - 1)$  related to the (negative) excess absorption of the solute. The terahertz dynamic hydration number is defined, in analogy with eq 4, as  $\nu_{\text{dyn}}^{\text{THz}} \equiv \nu_H(\xi_{\text{THz}} - 1)$ , where  $\xi_{\text{THz}} \equiv \alpha_H/\alpha_0$  is the terahertz dynamic perturbation factor (DPF).

Figure 10 shows the dielectric absorption coefficient measured on trehalose solutions at 20 °C by Heyden et al.<sup>26</sup> For the linear fit we have included the smallest number of points required to obtain a well-defined slope. This range ( $C \leq 0.3$  M) corresponds roughly to the independent hydration regime seen in our  $^{17}\text{O}$  data (Figure 7). The fit yields a slope of  $-58.8 \pm 9.4 \text{ cm}^{-1} \text{ M}^{-1}$  and an intercept of  $421.2 \pm 2.1 \text{ cm}^{-1}$ , consistent with the value  $420 \text{ cm}^{-1}$  measured on a pure water sample.<sup>26</sup> Dividing the slope by  $\alpha_0 V_W$  and subtracting<sup>26</sup>  $\delta_T = (206.85/18.047)(53/420 - 1) = -10.02$ , one obtains  $\nu_{\text{dyn}}^{\text{THz}} = 2.3 \pm 1.2$ . If the dynamic perturbation is attributed to the first hydration layer only (with  $\nu_H = 47$ ),  $\nu_{\text{dyn}}^{\text{THz}}$  corresponds to a terahertz DPF of  $\xi_{\text{THz}} = 1.05 \pm 0.03$ . If two hydration layers are perturbed, as argued by Heyden et al.,<sup>26</sup> one obtains (with  $\nu_H \approx 150$ )  $\xi_{\text{THz}} \approx 1.015 \pm 0.008$ . Because the second layer should be much less perturbed than the first layer, this result implies that

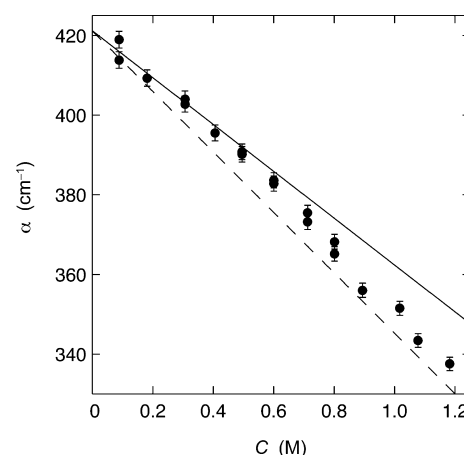


**Figure 10.** Dielectric absorption coefficient at 2.1–2.8 THz versus trehalose concentration in aqueous solution at 293.2 K.<sup>26</sup> The solid line resulted from a linear fit, according to eq 8, to the data in the dilute regime ( $C \leq 0.3$  M). The dashed line represents the ideal (no solvent perturbation) limit.

the second hydration layer differs by less than 1% from bulk water in its terahertz absorption. Such a small perturbation is not likely to have significant consequences.

Because the solute-induced perturbation of  $\alpha$  is so small, terahertz absorption is much less sensitive than  $^{17}\text{O}$  relaxation as a probe of hydration dynamics. In the ideal limit, where the solute does not perturb the water dynamics at all,  $\alpha(C)$  would decrease linearly with  $C$  (the dashed line in Figure 10) whereas  $R_1(C) = R_1^0$  would be independent of  $C$ . The deviation of the measured  $\alpha$  from this ideal limit is comparable to the experimental uncertainty in  $\alpha$  (Figure 10), whereas the corresponding  $R_1$  deviation from a horizontal line in Figure 7 is highly significant (for example, 50 times the error bar at  $C = 1$  M).

The two-layer range proposed by Heyden et al. (and described as a “long-range” effect)<sup>26</sup> was arrived at by attributing the weak nonlinearity in Figure 10 to hydration shell overlap, modeled by assuming a uniform distribution of trehalose molecules in a continuum solvent. This crude model ignores the dominant role of H-bonding for the structure of water and aqueous solutions and the consequent formation of branched trehalose networks.<sup>42</sup> Disregarding the three points below 0.2 M, the data in Figure 10 do not show a statistically significant deviation from a straight line (Figure S10, Supporting Information). Moreover, the slope of this line does not differ significantly from the slope of the ideal (dashed) line. In other words, the data do not indicate any significant terahertz solvent perturbation (the linear fit in Figure S10 (Supporting Information) yields  $\nu_{\text{dyn}}^{\text{THz}} = -0.12 \pm 0.24$ ) in the concentration range 0.2–1.2 M, where concentration-dependent trehalose clustering is indicated by the MD simulations of Sapir and Harries<sup>42</sup> and by the trehalose tumbling time (Figure S5).

It should be noted that the nonlinearities evident in Figures 7 and 10 are of opposite sense.  $R_1(C)$  reports a *larger*  $\nu_{\text{dyn}}$  at high  $C$ , which we ascribe to a strong slowing down of a subset of confined water molecules (increased  $\xi$ ) that overshadows the geometric effect of (first) hydration layer overlap (reduced  $\nu_H$ ). In contrast,  $\alpha(C)$  yields a *smaller*  $\nu_{\text{dyn}}^{\text{THz}}$  at high  $C$  (manifested as a smaller positive contribution to the increasingly negative slope), which Heyden et al. ascribe entirely to the geometric

overlap effect (reduced  $\nu_{\text{H}}$ ). In doing so, they assume that the terahertz absorption has the same value  $\alpha_{\text{H}}$  for confined water (overlapping hydration shells) as in a free hydration shell (surrounded by bulk water). However, it seems likely that the difference in  $\alpha_{\text{H}}$  between these environments is larger than the (subpercent) difference in  $\alpha_{\text{H}}$  between the second hydration layer and bulk water.

In conclusion, we do not believe that the terahertz absorption data of Heyden et al. can be used to determine the range of the solvent perturbation. Furthermore, the weak perturbation of collective vibrational dynamics in the solvent suggested by terahertz absorption measurements is likely to be of less consequence than the order-of-magnitude larger perturbation of the structural dynamics studied here.

## ■ CONCLUDING REMARKS

**Trehalose Self-Association.** The clustering of trehalose in aqueous solution has been studied in detail by MD simulations.<sup>40,42</sup> Solute clustering results from a subtle balance of solute–solute, solvent–solvent, and solute–solvent interactions and it is not clear if current force fields are sufficiently realistic to describe trehalose clustering accurately. Experimental results provide the necessary benchmarks against which the quality of simulation results should be judged. The single-molecule tumbling time  $\tau_{\text{R}}$  is a sensitive probe of solute–solute interactions and the present results (Figure 5) confirm the importance of self-association, revealing effects of trehalose–trehalose interactions even at 25 mM, below the concentrations examined by MD simulations.<sup>40,42</sup> The linear concentration dependence of  $\tau_{\text{R}}$  seen up to  $\sim 0.3$  M cannot be explained by hydrodynamic interactions but require direct trehalose–trehalose interactions (presumably H-bonds), as seen in MD simulations.<sup>40,42</sup> We did not attempt to interpret the nonlinear variation of  $\tau_{\text{R}}$  at higher concentrations in terms of a specific solution structure, but the finding that  $\tau_{\text{R}}$  scales with the macroscopic solution (rather than solvent) viscosity up to  $\sim 0.75$  M appears to be more consistent with transient clustering than with long-lived oligomers.<sup>39</sup> (If the solution contained a mixture of noninteracting oligomers, the solution viscosity should increase linearly with the total trehalose concentration as long as the oligomer shape does not change with concentration.) The scaling of  $\tau_{\text{R}}$  with solution viscosity breaks down in the concentration range where MD simulations find percolating trehalose clusters.<sup>40,42</sup>

**Hydration Dynamics.** Although solute–solute interactions are manifested in the trehalose tumbling time down to 25 mM, the effect of trehalose on the solvent's structural dynamics, as probed here by the single-molecule rotational correlation (closely related to the H-bond exchange time), is linear up to  $\sim 0.25$  M (Figure 7). From data in this independent hydration regime, we obtained the dynamic perturbation factor (DPF) that specifies the relative slowing down of water rotation (and H-bond exchange) in the hydration layer of trehalose (Figure 8). This DPF,  $1.60 \pm 0.02$  at 298 K, is in the same range as previously determined for other small organic solutes. As regards solvent perturbation, trehalose is virtually indistinguishable from other disaccharides, as previously concluded from  $^{17}\text{O}$  relaxation<sup>23,70</sup> and MD simulation<sup>39</sup> studies. The temperature dependence of the DPF, determined from 236 to 293 K (Figure 8), shows the same pronounced maximum as previously seen for other less polar solutes<sup>45</sup> and which appears because the activation energy for structural water dynamics is nearly constant in the hydration layer whereas, for bulk water, it

increases strongly in the supercooled regime. In conclusion, (monomeric) trehalose does not perturb water dynamics more than many other small organic molecules.

**Heterogeneous Hydration Dynamics.** The DPF varies considerably among different sites,<sup>43</sup> but the DPF reported here is the average over all water molecules in the hydration layer. MD simulations indicate that the DPF may be as large as 3 (at 300 K) for the dozen or so water molecules that H-bond to the hydroxyl groups of trehalose,<sup>39</sup> but most of the 47 water molecules that coat the surface of trehalose do not interact strongly with the solute. A more recent MD simulation reports DPFs in the range 1.4–3.3 for water molecules within 3.5 Å of any of the hydroxyl oxygens.<sup>43</sup> A larger DPF of 3–4 was found for water near the glycosidic oxygen,<sup>43</sup> but the water density here is so low that this site hardly contributes to the average DPF. It should be noted that the DPFs computed in these MD studies do not correspond (even after averaging over the hydration layer) to the experimentally derived DPF, so the comparison can at best be semiquantitative. In view of the heterogeneity of hydration dynamics, our finding that the average DPF is nearly the same for trehalose and many other solutes, some of which are distinctly hydrophobic, may be fortuitous to some extent. Furthermore, this coincidence does not mean that the mechanism of slowing down is precisely the same for all these solutes. For hydrophobic solutes, the main effect is the reduced H-bond exchange probability for a water molecule with fewer potential H-bond partners nearby.<sup>43,45,76,77</sup> For trehalose, this pure excluded-volume effect is combined with the effect of H-bond partners (notably, the 8 hydroxyl groups) on a rigid solute that cannot participate in the same kind of concerted H-bond exchange that occurs in bulk water.<sup>65</sup>

**Range of Solvent Perturbation.** At higher concentrations, the effect of trehalose on water structural dynamics shows a superlinear concentration dependence (Figure 7), implying that the expected stronger slowing down of water molecules confined in trehalose clusters dominates over the purely geometric effect of hydration-shell overlap (which reduces the number of water molecules that interact directly with trehalose). In contrast, the dielectric absorption coefficient  $\alpha(\text{C})$  in the 2.1–2.8 THz range<sup>26</sup> shows a sublinear concentration dependence of the perturbation induced by trehalose on subpicosecond collective solvent vibrations (Figure 10). This opposite deviation from linearity was attributed by Heyden et al. solely to geometric hydration-shell overlap, which they modeled in a way that seemed to imply a more “long-ranged” solvent perturbation.<sup>26</sup> However, we have argued here that the range of the very small perturbation of terahertz solvent dynamics cannot be determined from these dielectric absorption data.

In discussing the range of the solvent perturbation, it should be recognized that hydration numbers with different meanings are in use. Some authors identify the hydration number with the water molecules that H-bond to the solute or with the water molecules that reside within 3.0 or 3.5 Å of a solute oxygen atom. If this number, which is in the range 10–30 for trehalose,<sup>37–39</sup> is identified as the first hydration layer, then water molecules next to the solute's carbon atoms will be counted in the second layer.<sup>39</sup> (The C–O<sub>w</sub> pair correlation function typically peaks at 3.5–3.8 Å with the first minimum at 4.5–5.5 Å.) In contrast, here we use a purely geometric hydration layer, identified as the number of water molecules required to cover the solute with one layer. Without a priori knowledge about which sites are most perturbed for a given

solute, it seems sensible to attribute the average DPF to all molecules in the first layer. Furthermore, it should be kept in mind that the step-function (or two-state) model of the perturbation is a simplification. When we attribute the perturbation of water rotational dynamics to the first layer (it is then 67%), we do not imply that the second layer is exactly like bulk, but simply that it is much less perturbed (say, < 10% slow-down compared to bulk) than the first layer.

**Second-Order Dynamic Coupling.** The first-order dynamic coupling between solute and solvent is expressed in the SED relation as a proportionality between solute tumbling time and solvent viscosity. The second-order coupling, which arises because the solute modifies the solvent, is usually modeled by incorporating “bound” water molecules in the hydrodynamic volume (leading to yet another operationally defined “hydration number”). Because the hydration layer is highly mobile, with water molecules exchanging with the bulk on a 10 ps time scale, this “iceberg” model is misleading for small solutes as well as for proteins.<sup>61</sup> Using a more general local viscosity model, we predict that the second-order solvent effect (the deviation from the SED relation) should exhibit the same temperature dependence (with a pronounced maximum near 260 K) as the solvent DPF. By combining <sup>2</sup>H trehalose and <sup>17</sup>O water relaxation data from the same sample, we demonstrated that this is the case for trehalose (Figure 9) and presumably for other solutes as well.

**Protein Stabilization.** What are the implications of the present findings for the mechanism of protein stabilization by trehalose? Hydration dynamics (the rate of water motions) cannot be causally linked with protein stability (the difference in free energy between native and unfolded states), but, to the extent that dynamics can be used as a proxy for structure and energetics in the hydration layer, there may well be a correlation. We have only examined trehalose here, but previous comparisons of the hydration dynamics of trehalose with that of other disaccharides does not provide any grounds for attributing trehalose’s superior protein-stabilizing capacity to its hydration. Because the unfolded protein exposes a much larger surface to the solvent, it seems likely that trehalose exerts its effect mainly on that state. A key question would then be how the unfolded protein affects the open and branched network of self-interacting trehalose molecules. However, if trehalose clustering plays a role in protein stabilization, one would not expect the stabilization free energy to increase linearly with trehalose concentration up to ~1 M (Figure S11, Supporting Information).<sup>6</sup>

## ■ ASSOCIATED CONTENT

### ■ Supporting Information

Preparation and characterization of deuterated trehalose (S1), paramagnetic relaxation enhancement (S2), trehalose concentration determination (S3), control experiments on emulsion samples (S4), temperature-dependent hydration dynamics (S5), terahertz dielectric absorption (S6), protein stabilization by trehalose (S7). This material is available free of charge via the Internet at <http://pubs.acs.org>.

## ■ AUTHOR INFORMATION

### Corresponding Author

\*E-mail: [bertil.halle@bpc.lu.se](mailto:bertil.halle@bpc.lu.se). Phone: +46 (0)46 222 9516.

### Notes

The authors declare no competing financial interest.

## ■ ACKNOWLEDGMENTS

We thank Peter Immerzeel for performing the anion exchange chromatography and Filip Persson for hydrodynamic computations. This work was supported by grants from the Swedish Research Council, the Crafoord Foundation and the Knut & Alice Wallenberg Foundation.

## ■ REFERENCES

- (1) Van Laere, A. *FEMS Microbiol. Rev.* **1989**, *63*, 201–210.
- (2) Elbein, A. D.; Pan, Y. T.; Pastuszak, I.; Carroll, D. *Glycobiology* **2003**, *13*, 17R–27R.
- (3) Jain, N. K.; Roy, I. *Protein Sci.* **2009**, *18*, 24–36.
- (4) Burg, M. B.; Ferraris, J. D. *J. Biol. Chem.* **2008**, *283*, 7309–7313.
- (5) Arakawa, T.; Timasheff, S. N. *Biochemistry* **1982**, *21*, 6536–6544.
- (6) Xie, G. F.; Timasheff, S. N. *Biophys. Chem.* **1997**, *64*, 25–43.
- (7) Kaushik, J. K.; Bhat, R. *J. Biol. Chem.* **2003**, *278*, 26458–26465.
- (8) Auton, M.; Rösgen, J.; Sinev, M.; Holthauzen, L. M. F.; Bolen, D. W. *Biophys. Chem.* **2011**, *159*, 90–99.
- (9) Crowe, J. H.; Hoekstra, F. A.; Crowe, L. M. *Annu. Rev. Physiol.* **1992**, *54*, 579–599.
- (10) Sakurai, M.; Furuki, T.; Akao, K.; Tanaka, D.; Nakahara, Y.; Kikawada, T.; Watanabe, M.; Okuda, T. *Proc. Natl. Acad. Sci. U. S. A.* **2008**, *105*, 5093–5098.
- (11) Hengherr, S.; Worland, M. R.; Reuner, A.; Brümmer, F.; Schill, R. O. *Physiol. Biochem. Zool.* **2009**, *82*, 749–755.
- (12) Hengherr, S.; Schill, R. O.; Clegg, J. S. *Physiol. Biochem. Zool.* **2011**, *84*, 249–257.
- (13) Chang, L.; Pikal, M. J. *J. Pharm. Sci.* **2009**, *98*, 2886–2908.
- (14) Kamerzell, T. J.; Esfandiary, R.; Joshi, S. B.; Middaugh, C. R.; Volkin, D. B. *Adv. Drug Delivery Rev.* **2011**, *63*, 1118–1159.
- (15) Yancey, P. H.; Clark, M. E.; Hand, S. C.; Bowlus, R. D.; Somero, G. N. *Science* **1982**, *217*, 1214–1222.
- (16) Record, M. T.; Courtenay, E. S.; Cayley, D. S.; Guttman, H. J. *Trends Biochem. Sci.* **1998**, *23*, 143–148.
- (17) Buitink, J.; Leprince, O. *Compt. Rend. Biol.* **2008**, *331*, 788–795.
- (18) Frank, G. A. *J. Phys. Chem. Ref. Data* **2007**, *36*, 1279–1285.
- (19) Peric-Hassler, L.; Hansen, H. S.; Baron, R.; Hünenberger, P. H. *Carbohydr. Res.* **2010**, *345*, 1781–1801.
- (20) Lins, R. D.; Pereira, C. S.; Hünenberger, P. H. *Proteins* **2004**, *55*, 177–186.
- (21) Lerbret, A.; Bordat, P.; Affouard, F.; Hédoux, A.; Guinet, Y.; Descamps, M. *J. Phys. Chem. B* **2007**, *111*, 9410–9420.
- (22) Liu, F.-F.; Ji, L.; Zhang, L.; Dong, X.-Y.; Sun, Y. *J. Chem. Phys.* **2010**, *132*, 225103.
- (23) Uedaira, H.; Ishimura, M.; Tsuda, S.; Uedaira, H. *Bull. Chem. Soc. Jpn.* **1990**, *63*, 3376–3379.
- (24) Karger, N.; Lüdemann, H.-D. *Z. Naturforsch. C* **1991**, *46*, 313–317.
- (25) Batta, G.; Kövér, K. E.; Gervay, J.; Hornyák, M.; Roberts, G. M. *J. Am. Chem. Soc.* **1997**, *119*, 1336–1345.
- (26) Heyden, M.; Bründemann, E.; Heugen, U.; Niehues, G.; Leitner, D. M.; Havenith, M. *J. Am. Chem. Soc.* **2008**, *130*, 5773–5779.
- (27) Pagnotta, S. E.; Alegria, A.; Colmenero, J. *Phys. Chem. Chem. Phys.* **2012**, *14*, 2991–1996.
- (28) Paolantoni, M.; Comez, L.; Gallina, M. E.; Sassi, P.; Scarponi, F.; Fioretto, D.; Morresi, A. *J. Phys. Chem. B* **2009**, *113*, 7874–7878.
- (29) Gallina, M. E.; Comez, L.; Morresi, A.; Paolantoni, M.; Perticaroli, S.; Sassi, P.; Fioretto, D. *J. Chem. Phys.* **2010**, *132*, 214508.
- (30) Lerbret, A.; Bordat, P.; Affouard, F.; Guinet, Y.; Hédoux, A.; Paccou, L.; Prévost, D.; Descamps, M. *Carbohydr. Res.* **2005**, *340*, 881–887.
- (31) Malsam, J.; Aksan, A. *J. Phys. Chem. B* **2009**, *113*, 6792–6799.
- (32) Faraone, A.; Magazà, S.; Lechner, R. E.; Longeville, S.; Maisano, G.; Majolino, D.; Migliardo, P.; Wanderlingh, U. *J. Chem. Phys.* **2001**, *115*, 3281–3286.
- (33) Magazú, S.; Villari, V.; Migliardo, P.; Maisano, G.; Telling, M. T. *F. J. Phys. Chem. B* **2001**, *105*, 1851–1855.



- (34) Köper, I.; Bellissent-Funel, M.-C.; Petry, W. *J. Chem. Phys.* **2005**, *122*, 014514.
- (35) Pagnotta, S. E.; McLain, S. E.; Soper, A. K.; Bruni, F.; Ricci, M. A. *J. Phys. Chem. B* **2010**, *114*, 4904–4908.
- (36) Liu, Q.; Schmidt, R. K.; Teo, B.; Karplus, P. A.; Brady, J. W. *J. Am. Chem. Soc.* **1997**, *119*, 7851–7862.
- (37) Bonnanno, G.; Noto, R.; Fornili, S. L. *J. Chem. Soc., Faraday Trans.* **1998**, *94*, 2755–2762.
- (38) Engelsens, S. B.; Pérez, S. J. *Phys. Chem. B* **2000**, *104*, 9301–9311.
- (39) Lee, S. L.; Debenedetti, P. G.; Errington, J. R. *J. Chem. Phys.* **2005**, *122*, 204511.
- (40) Lerbret, A.; Bordat, P.; Affouard, F.; Descamps, M.; Migliardo, P. *J. Phys. Chem. B* **2005**, *109*, 11046–11057.
- (41) Lerbret, A.; Affouard, F.; Bordat, P.; Hédoux, A.; Guinet, Y.; Descamps, M. *J. Non-Cryst. Solids* **2011**, *357*, 695–699.
- (42) Sapir, L.; Harries, D. *J. Phys. Chem. B* **2011**, *115*, 624–634.
- (43) Verde, A. V.; Campen, R. K. *J. Phys. Chem. B* **2011**, *115*, 7069–7084.
- (44) Rasmussen, D. H.; MacKenzie, A. P. *J. Chem. Phys.* **1973**, *59*, 5003–5013.
- (45) Qvist, J.; Halle, B. *J. Am. Chem. Soc.* **2008**, *130*, 10345–10353.
- (46) Koch, H. J.; Stuart, R. S. *Carbohydr. Res.* **1977**, *59*, C1–C6.
- (47) Abragam, A. *The Principles of Nuclear Magnetism*; Clarendon Press: Oxford, U.K., 1961.
- (48) Bose-Basu, B.; Zajicek, J.; Bondo, G.; Zhao, S.; Kubsch, M.; Carmichael, I.; Serianni, A. S. *J. Magn. Reson.* **2000**, *144*, 207–216.
- (49) Nunes, S. C. C.; Jesus, A. J. L.; Moreno, M. J.; Eusébio, M. E. S. *Carbohydr. Res.* **2010**, *345*, 2048–2059.
- (50) Nagase, H.; Ogawa, N.; Endo, T.; Shiro, M.; Ueda, H.; Sakurai, M. *J. Phys. Chem. B* **2008**, *112*, 9105–9111.
- (51) McCain, D. C.; Markley, J. L. *J. Am. Chem. Soc.* **1986**, *108*, 4259–4264.
- (52) McCain, D. C.; Markley, J. L. *J. Magn. Reson.* **1987**, *73*, 244–251.
- (53) Effemey, M.; Lang, J.; Kowalewski, J. *Magn. Reson. Chem.* **2000**, *38*, 1012–1018.
- (54) Baraguey, C.; Mertens, D.; Dölle, A. *J. Phys. Chem. B* **2002**, *106*, 6331–6337.
- (55) Ortega, A.; Amorós, D.; García de la Torre, J. *Biophys. J.* **2011**, *101*, 892–898.
- (56) Halle, B. *J. Chem. Phys.* **2009**, *131*, 224507.
- (57) Hallett, J. *Proc. Phys. Soc.* **1963**, *82*, 1046–1050.
- (58) Cho, C. H.; Urquidi, J.; Singh, S.; Robinson, G. W. *J. Phys. Chem. B* **1999**, *103*, 1991–1994.
- (59) Qvist, J.; Mattea, C.; Sunde, E. P.; Halle, B. *J. Chem. Phys.* **2012**, *136* (204505), 1–16.
- (60) Banipal, P. K.; Banipal, T. S.; Lark, B. S.; Ahluwalia, J. C. *J. Chem. Soc., Faraday Trans.* **1997**, *93*, 81–87.
- (61) Halle, B.; Davidovic, M. *Proc. Natl. Acad. Sci. U. S. A.* **2003**, *100*, 12135–12140.
- (62) Meng, E. C.; Kollman, P. A. *J. Phys. Chem.* **1996**, *100*, 11460–11470.
- (63) Jones, R. B. *Physica A* **1989**, *157*, 752–768.
- (64) Magazú, S.; Maisano, G.; Migliardo, P.; Villari, V. *J. Chem. Phys.* **1999**, *111*, 9086–9092.
- (65) Laage, D.; Hynes, J. T. *J. Phys. Chem. B* **2008**, *112*, 14230–14242.
- (66) Rossky, P. J.; Karplus, M. *J. Am. Chem. Soc.* **1979**, *101*, 1913–1937.
- (67) Vaisman, I. I.; Brown, F. K.; Tropsha, A. *J. Phys. Chem.* **1994**, *98*, 5559–5564.
- (68) Paschek, D. *J. Chem. Phys.* **2004**, *120*, 10605–10617.
- (69) Fraczekiewicz, R.; Braun, W. *J. Comput. Chem.* **1998**, *19*, 319–333.
- (70) Uedaira, H.; Ikura, M.; Uedaira, H. *Bull. Chem. Soc. Jpn.* **1989**, *62*, 1–4.
- (71) Kawai, H.; Sakurai, M.; Inoue, Y.; Chûjô, R.; Kobayashi, S. *Cryobiology* **1992**, *29*, 599–606.
- (72) Venable, R. M.; Hatcher, E.; Guvench, O.; MacKerell, A. D.; Pastor, R. W. *J. Phys. Chem. B* **2010**, *114*, 12501–12507.
- (73) Miller, D. P.; de Pablo, J. J.; Corti, H. *Pharm. Res.* **1997**, *14*, 578–590.
- (74) Mattea, C.; Qvist, J.; Halle, B. *Biophys. J.* **2008**, *95*, 2951–2963.
- (75) Weingärtner, H.; Knocks, A.; Boresch, S.; Höchtl, P.; Steinhauser, O. *J. Chem. Phys.* **2001**, *115*, 1463–1472.
- (76) Sciortino, F.; Geiger, A.; Stanley, H. E. *J. Chem. Phys.* **1992**, *96*, 3857–3865.
- (77) Laage, D.; Stirnemann, G.; Hynes, J. T. *J. Phys. Chem. B* **2009**, *113*, 2428–2435.